Supporting Materials of "Few-layer α-Sb₂O₃ molecular crystal as high-*k* van der Waals dielectric: electronic decoupling and significant surface ionic behaviors"

Jia-Bin Liu[1], Fu-Sheng Zhang[1], Shu-Hui Wang[1], Kai-Lang Liu[2], Rui-Chun Xiao[3], Chen-Dong Jin[1], Hu Zhang[1], Ru-Qian Lian[1], Rui-Ning Wang[1], Peng-Lai Gong[1,*], Xing-Qiang Shi[1] and Jiang-Long Wang[1]

[1]Key Laboratory of Optic-Electronic Information and Materials of Hebei Province, Hebei Research Center of the Basic Discipline for Computational Physics, College of Physics Science and Technology, Hebei University, Baoding 071002, P. R. China

[2]State Key Laboratory of Material Processing and Die & Mould Technology, School of Material Sciences and Engineering, Huazhong University of Science and Technology, Wuhan, China

[3] Institute of Physical Science and Information Technology, Anhui University, Hefei, 230601, China

*E-mails: gongpl@hbu.edu.cn

Contents

5

1. Definition of several 2D thicknesses and the effect of the thickness on the dielectric constant

8
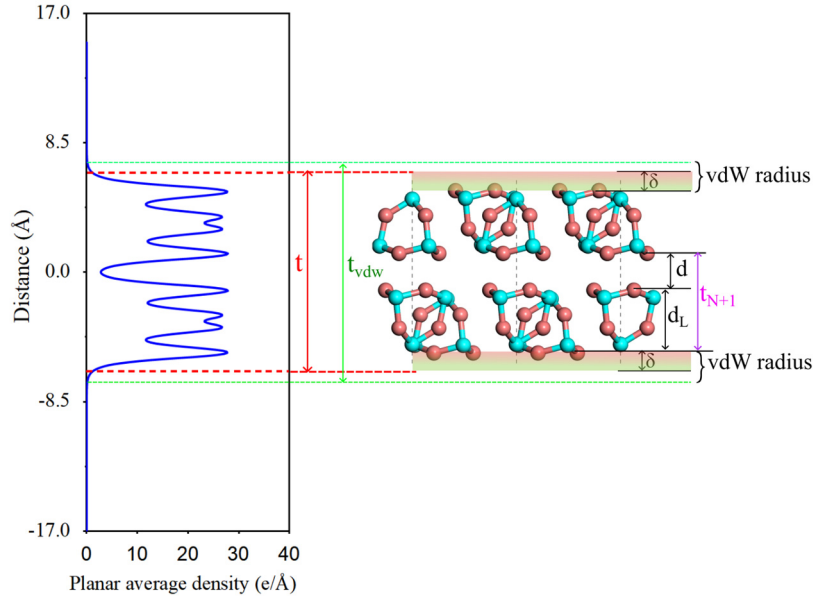
Fig. S1: Various definitions of the slab thickness for few-layer Sb$_2$O$_3$. The total slab thickness (t) is the vertical distance between the outermost atoms of the slab, plus the region of charge spillover (δ) extending beyond the outermost atomic layers where the charge density falls to approximately 5% of the nearest peak values. δ represents the region of charge spillover extending beyond the outermost atomic layers, and it does not vary significantly with different numbers of layers. Considering the vdW radius of the outermost O atoms, we define the thickness of the slab as t_{vdW}. The total thickness of N layer is defined by the thickness of $N+1$ layers (i.e., $N \times$ one-layer thickness $+ N \times$ interlayer spacing), denoted as t_{N+1}, where the one-layer thickness (d_L) represents the vertical distance between the outermost atoms in each layer, and the interlayer spacing (d) represents the vdW gap between adjacent layers. The descending order of the three slab thicknesses is $t_{vdW} > t > t_{N+1}$.

21

22
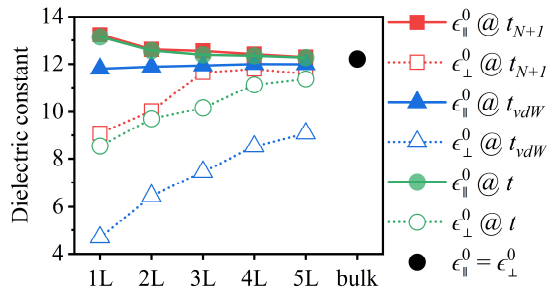
Fig. S2: Influence of the slab thickness definitions on the dielectric constant. Three different slab thickness definitions for the few-layer Sb_2O_3 exhibit different effects on the in-plane and out-of-plane static dielectric constant. Here, the influence of vacuum on the dielectric constant has been removed. When employing the thickness defined as t_{N+1}, it is observed that the out-of-plane dielectric constant decreases after exceeding 4L; when using the thickness defined as t_{vdw}, the in-plane dielectric constant shows a slight increase, but it remains smaller than the bulk value. This behavior is notably distinct from that observed with t_{N+1} and t. The observations above suggest that a well-defined slab thickness is essential for elucidating the underlying physical principles. We define the slab thickness based on the charge density decay, considering interlayer interactions and surface effects within the current system. This definition falls between the values of t_{vdW} and t_{N+1}. The figure demonstrates that our definition mitigates oscillating decay resulting from numerical noise and the risk of deviating from bulk properties.

2. Lattice dynamic stability
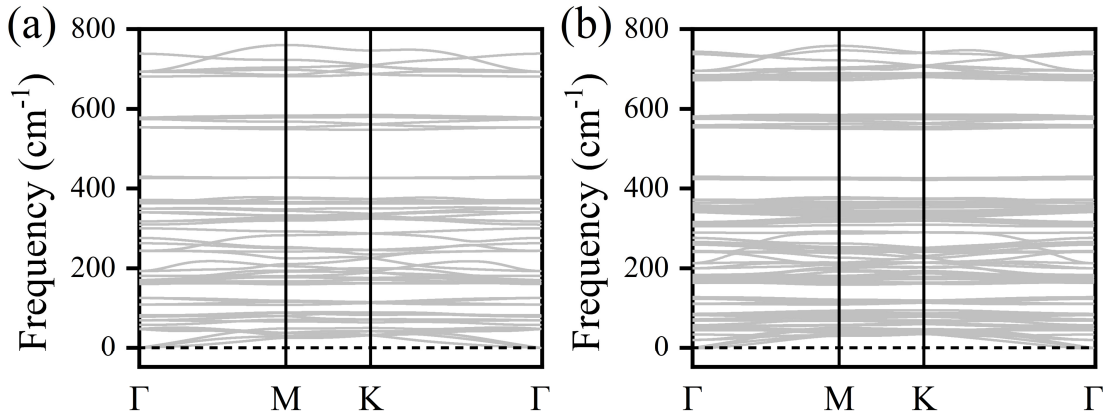
Fig. S3: Phonon spectra of monolayer and bilayer α-Sb_2O_3. Their phonon spectra display no imaginary frequencies, affirming the dynamical stability of the material.

3. Thermodynamic stability
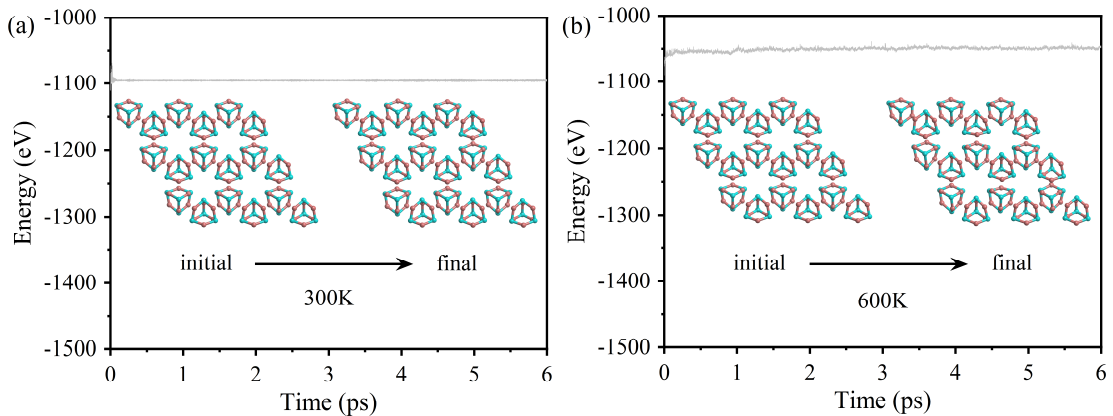
Fig. S4: First-principles molecular dynamics of monolayer α-Sb$_2$O$_3$. Total energy evolution of monolayer α-Sb$_2$O$_3$ over time (a) at 300 K (b) 600 K. The illustration in figures is structure evolution from initial to final states. The total simulation time is 6 ps, with a time step of 1 fs.

4. The effect of spin-orbit coupling (SOC) on the band gap
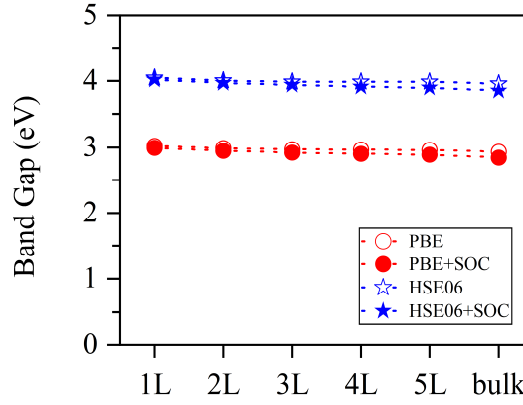
Fig. S5: Band gap as a function of layer number at various computational levels. Computational methods employed here include PBE, PBE+SOC, HSE06, and HSE06+SOC. It is observed that the band gap exhibits a gradual decrease as the layer number increases, and this behavior is consistent across all computational methods. The influence of the SOC effect on the band gap is minimal, leading us to exclude SOC effects from our calculations.

5. Schematic diagram of band splitting
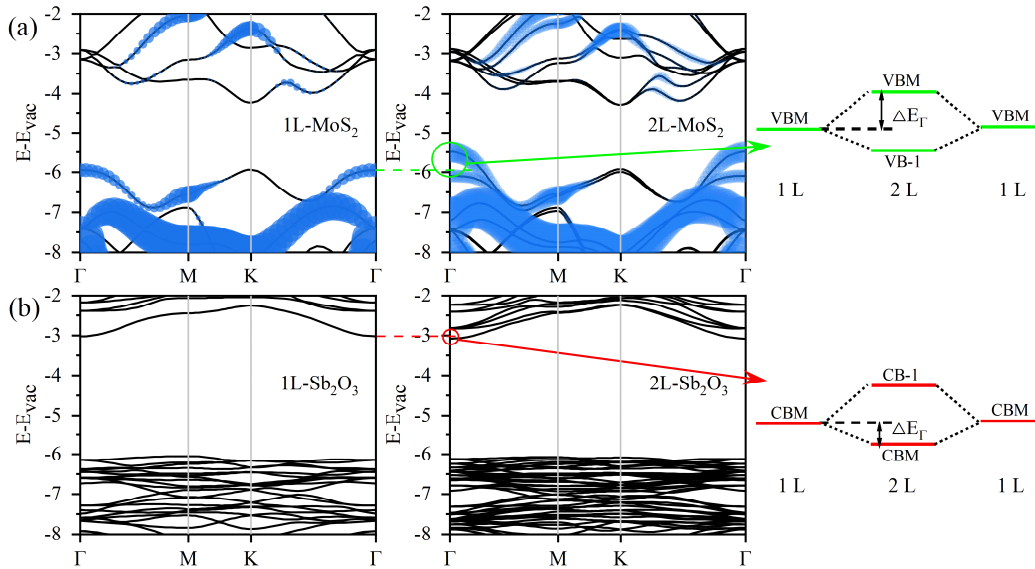
Fig. S6: a) The band structure of monolayer and bilayer MoS$_2$ projected by S-p_z orbitals and the schematic representation of band splitting of the VBM induced by interlayer QB interaction. b) The band structure of monolayer and bilayer Sb$_2$O$_3$ and the schematic representation of band splitting of the CBM induced by interlayer QB interaction.

$\triangle E \propto t$ $\triangle E \propto t$ $\triangle E \propto (t)^2/E_{diff}$
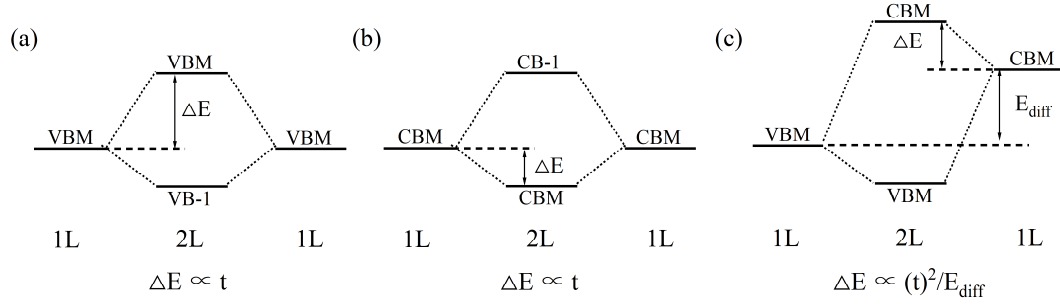
Fig. S7: The energy level distribution diagrams of three orbital interactions caused by the interlayer QB interactions. a) Occupied-occupied interaction for band splitting schematic. b) Unoccupied-unoccupied interaction for band splitting schematic. c) Occupied-unoccupied interaction for band splitting schematic.

6. Projected band structure monolayer and bilayer α-Sb₂O₃
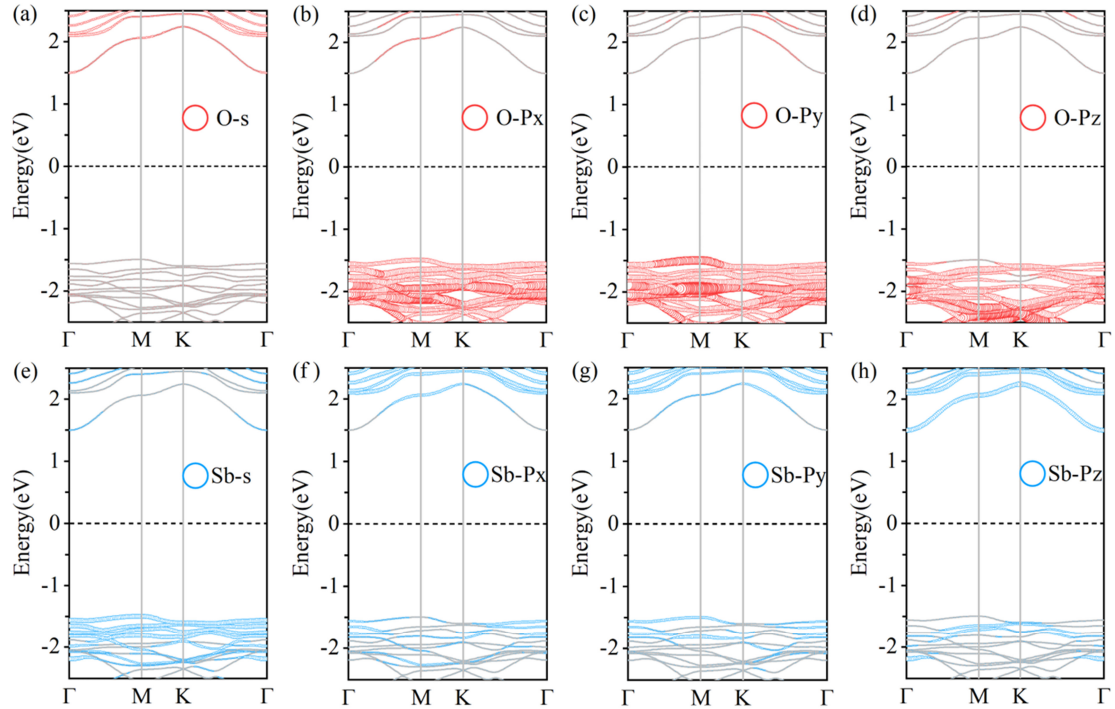
Fig. S8: Projected energy band structures of the monolayer α-Sb$_2$O$_3$ using the PBE method. a) Projected band of s, p_x, and p_y and p_z orbitals of O atoms; b) Projected band of s, p_x, p_y, and p_z orbit of Sb atoms. It is evident that the CBM is primarily contributed by Sb-5p_z, and the VBM is mainly contributed by the O-2p_x, O-2p_y, and Sb-5s orbitals. This observation holds for the bilayer as well.
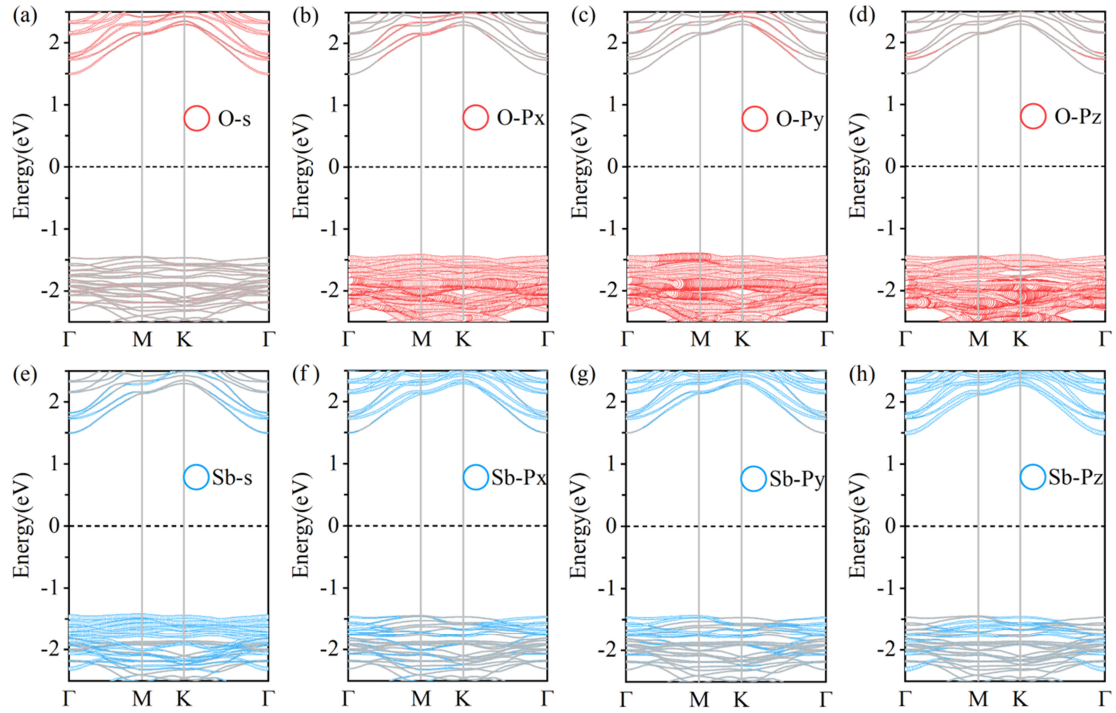
Fig. S9: Projected energy band structures of the bilayer α-Sb$_2$O$_3$ using the PBE method. a) Projected band of s, p_x, and p_y and p_z orbitals of O atoms; b) Projected band of s, p_x, p_y, and p_z orbit of Sb atoms.

7. The HSE band structures of α-Sb$_2$O$_3$ with the layer number range from 3 to 5, monolayer TMDs, and monolayer BP
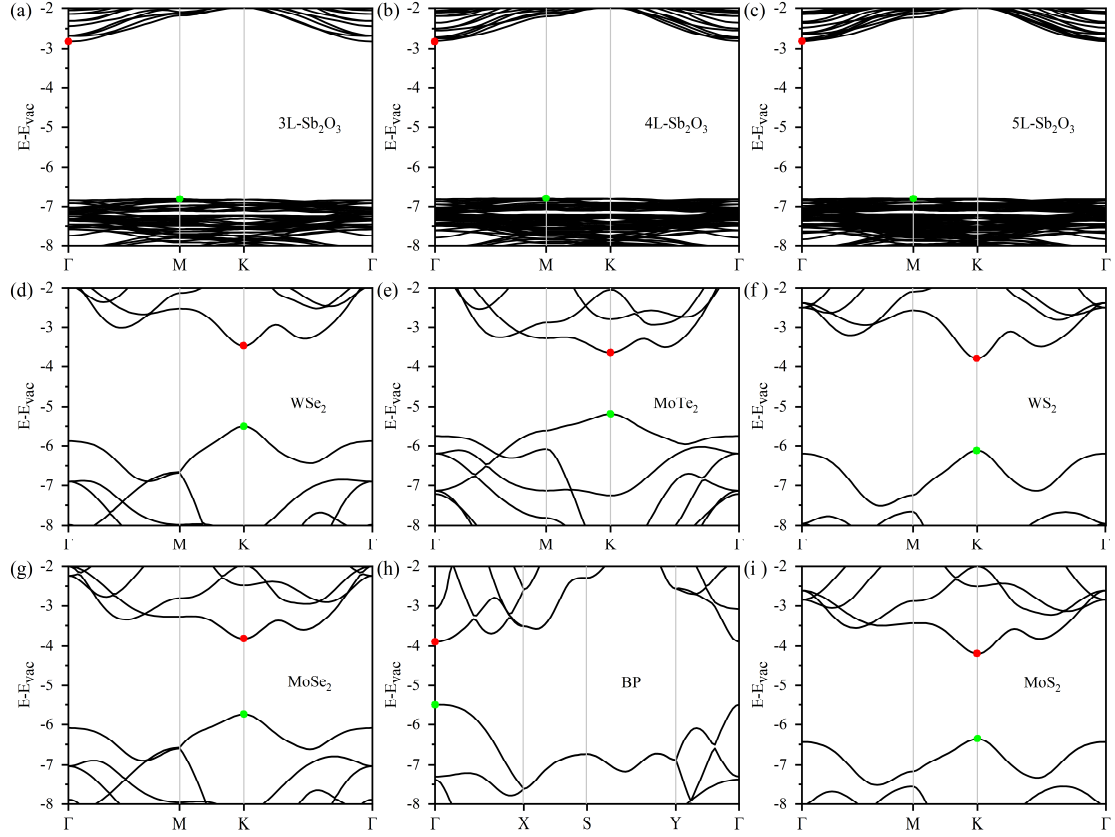
Fig S10: The band structures of α-Sb_2O_3 with the layer number range from 3 to 5, monolayer TMDs, and monolayer BP using the HSE06 method. The CBM (VBM) positions are marked with red (green) spheres in the band diagrams. The energy levels of these band diagrams are referenced to the vacuum level.

8. Band edge alignment in the heterojunction while considering the interface interaction

The VBO and CBO values for isolated Sb_2O_3 and MoS_2 are 0.41 and 1.45 eV, respectively. Our calculations reveal that the interface interaction results in an increase of approximately 0.136 eV in the VBO of the heterojunction. This increase is attributed to contributions from the interfacial dipole moment (+0.10 eV) and interlayer QB effect (+0.036 eV). The influence of interface interaction on the CBO is slightly smaller, resulting in a reduction of 0.042 eV. This reduction is attributed to the competitive behavior between the interfacial dipole moment (-0.10 eV) and interlayer QB effect (+0.058 eV). It is worth noting that the interfacial dipole effect can be determined by calculating the step height within the vacuum region from the planar-averaged electrostatic potential energy curve. We establish the vacuum energy level of the 2D semiconductor in the heterojunction as the reference energy level for the heterojunction.

This reference level solely influences the proportion of QB and interaction dipole contributions to the modification of the band offset without affecting the overall changes in CBO and VBO. The above results demonstrate that a small band offset has the potential to be corrected to some extent through interlayer interactions, and this correction can influence the leakage current values. In this case, the increase of VBO in Sb_2O_3/MoS_2 vdwH reduced the leakage current by two orders of magnitude. We further verified the influence of interface effects on the isolated large band offset. We observed that when the isolated band offset is larger than 0.67 eV (as in the case of Sb_2O_3/WS_2), the impact of interface interactions on band offset changes will not cause the already low leakage current to exceed the IRDS standard.
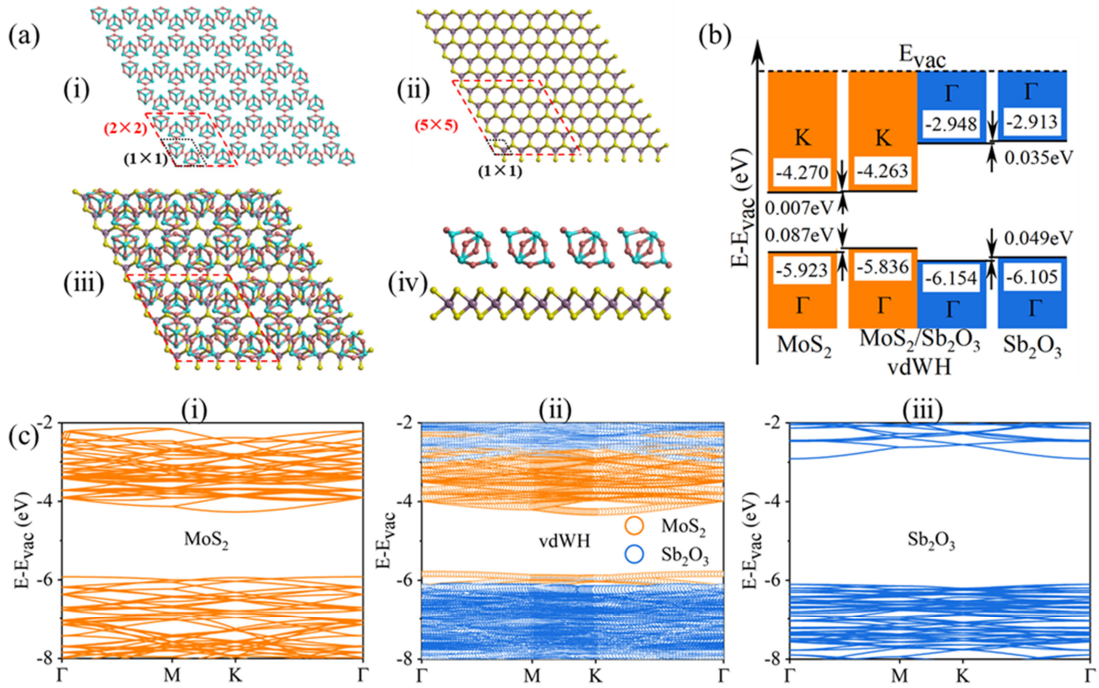
Fig. S11: (a) Geometric structure of α-Sb_2O_3/MoS_2 vdW heterostructure: top views of (i) α-Sb_2O_3 with the (1×1) and (2×2) cells labeled out; (ii) MoS_2 with (1×1) and (5×5) cells; (iii) and (iv) the top- and side views of the α-Sb_2O_3/MoS_2 vdW heterostructure (vdWH). (b) DFT-calculated band alignment of isolated MoS_2, α-Sb_2O_3/MoS_2 heterostructure, isolated α-Sb_2O_3 as shown with bars; (c) projected band structures for isolated MoS_2, α-Sb_2O_3/MoS_2 heterostructure, isolated α-Sb_2O_3, respectively. The energy reference is the vacuum levels (E_{vac}) of MoS_2, α-Sb_2O_3/MoS_2 heterostructure, isolated α-Sb_2O_3, respectively. In the vdW heterostructure, there are two vacuum levels on the α-Sb_2O_3 and MoS_2 sides, and the vacuum level on the MoS_2 side is set to zero.

9. Effect of various vdW corrections on geometry structures of bulk Sb$_2$O$_3$.

Among the various vdW corrections, we observed that the relaxed bulk lattice constants obtained through the D2-vdW method are in closest agreement with experimental results. Consequently, we selected the D2-vdW correction to optimize the structures of bulk α-Sb$_2$O$_3$ and its corresponding few layers.

Table S1: Impact of the different vdW corrections on the lattice constants of the bulk α-Sb$_2$O$_3$. Experimental data is included for reference.

vdW corrections	a=b=c (Å)	α=β=γ (°)
D2[1]	11.07	90
D3[2]	11.24	90
optB88-vdW[3]	11.06	90
SCAN+rvv10[4]	10.97	90
Expt.[5]	11.10	90

10. Interlayer binding energy

The vertical interlayer distance of α-Sb$_2$O$_3$ is ~2.4 Å, which is far smaller than that of conventional 2D materials such as graphene, h-BN, and MoS$_2$, etc. However, the vertical interlayer distance may not necessarily reflect the magnitude of interlayer binding energy. In 2012, R. M. Nieminen *et. al.* in their work ointed out that it was hard to find correlations of interlayer binding energy E_B to any other quantity in layered compounds. The quantities scanned for such correlations were the interlayer distances, intralayer thicknesses, band-gap/metallicity, and properties of the constituent atoms, such as the atomic weights and polarizabilities. The interlayer binding energy for many layered compounds is independent of the material's electronic structure, and they are around 20 meV/Å^2.

On the other hand, the interlayer binding energy strongly depends on the van der Waals (vdW) correction method used; therefore, we compared the binding energy calculated using different methods, where the binding energy calculation formula is $E_B=(nE_1-E_n)/(nA)$ (E_1 and E_n are the energies of monolayer and n-layer systems, and A is the surface area of the 2D unit cell). As shown in Table S2, for Sb$_2$O$_3$ and MoS$_2$, their binding energies generally vary within the range of 16-28 meV/Å^2. Among these, the SCAN+rvv10 scheme is generally considered more reliable and computationally efficient, with results close to the RPA method. It can be observed that for MoS$_2$, the

binding energies calculated by SCAN+rvv10 and RPA are in excellent agreement. Therefore, we consider the binding energy of Sb_2O_3 calculated based on SCAN+rvv10 (21.57 meV/$Å^2$) to be reliable data, close to the binding energy of MoS_2, reflecting the common trend of binding energies of the majority of two-dimensional materials being around 20 meV/$Å^2$. Thus, both belong to layered materials with weak interlayer interactions, although the interlayer perpendicular distance of the former is smaller than that of the latter.

Table S2: The interlayer binding energies of bulk α-Sb_2O_3 and bulk MoS_2 calculated using different van der Waals (vdW) methods.

vdW	interlayer binding energy (meV/ $Å^2$)	
	Sb_2O_3	MoS_2
D2[1]	27.06	16.12
D3[2]	18.74	28.61
DFT-DF[6]	15.77	18.34
DFT-DF2[7]	18.19	19.14
optB86-vdW[8]	24.56	26.04
optB88-vdW[3]	24.11	25.45
SCAN+rvv10[4]	21.57	19.67
RPA[9]	-	20.50 [10]

11. Decomposition of the interlayer QB interaction to band splitting

For the occupied-occupied orbital interactions (Fig. S7a) and unoccupied-unoccupied orbital interactions (Fig. S7b), the shits of band edges induced by QB (relative to monolayer) ΔE are approximately proportional to the hopping integral t. For the occupied-unoccupied interactions, ΔE is approximately proportional to t^2/E_{Diff} (Fig. S7c), where E_{Diff} is the energy difference before orbital hybridization. Therefore, by computing the interlayer orbital interactions of VBM and CBM in the bilayer (2L) through k-dependent Crystal Orbital Hamilton Population (k-COHP) [11] implemented in the LOBSTER package [12], we can reflect the numerical values of t and thus predict ΔE.

Our calculations reveal that the interlayer t values for the interlayer nearest neighbor Sb-O atoms and interlayer nearest neighbor O-O atoms in the VBM of 2L-Sb_2O_3 are exceedingly small, resulting in almost zero band edge variation ΔE (Table

S3); this situation similarly holds for the entire highest valence band. This is attributed to the dominance of in-plane O-$p_{x/y}$ orbitals and the large distance between interlayer O-$p_{x/y}$ orbitals, leading to the negligible interlayer t and, thus, the minimal variation of the highest valence band as the change of layer number.

For the CBM of $2L$-Sb_2O_3, the k-COHP of interlayer nearest neighbor Sb-Sb atoms and interlayer nearest neighbor Sb-O atoms are -0.0193 and +0.036 (Table S3), respectively. The former indicates the bonding character of Sb-Sb atoms, consistent with the normal two-level interaction picture (Fig. S7b). The latter reflects the antibonding character of Sb-O atoms, which does not conform to the normal two-level interaction picture, indicating the involvement of occupied-unoccupied interactions is necessary to explain this anomalous phenomenon. For occupied-unoccupied interactions, ΔE depends on the energy difference E_{Diff} between the initial energy levels of the VBM and CBM of the monolayer, as well as t^2 values. For Sb_2O_3, E_{Diff} is calculated to be 3.00 eV by PBE functional. Although the t value for occupied-unoccupied interactions is larger than that for occupied-occupied interactions, the significant magnitude of E_{Diff} results in ΔE being not particularly significant. Taking into account the periodicity of the crystal lattice, the equivalent number of the interlayer atom pairs mentioned above is 6. Therefore, the ΔE induced by the orbital interactions of Sb-O atoms and O-O atoms are -0.1158 and +0.0154 eV, respectively (the $\pm$ sign indicates the CBM relative to the 1L level rising and falling). This indicates that the bonding states formed by the nearest neighbor Sb-Sb interlayer mainly induce a CBM decrease of +0.1158 eV, which is close to the ΔE (~0.06 eV) directly computed using DFT. The slight differences between the two methods may arise from lattice/atom distortion or inherent shortcomings in the k-COHP itself. Furthermore, for large band gaps, the occupied-unoccupied interaction can often be safely neglected. The QB in CBM at $2L$ Sb_2O_3 is slightly stronger than that of VBM, mainly due to the domination of a small number of out-of-plane Sb-p_z orbitals in the CBM.

To demonstrate the universality of k-COHP in predicting ΔE, we computed the interlayer QB strong MoS_2 system. We found t value in MoS_2 to be an order of magnitude larger than that of Sb_2O_3, hence resulting in a significant ΔE. In detail, in the

11

VBM of 2L-MoS$_2$, the k-COHP of the nearest neighbor S-S atoms is -0.2144 (antibonding feature), as shown in Table S3, consistent with the picture of two-level interactions (Fig. S7a). Taking into account the periodicity of the crystal lattice, the equivalent number of atom pairs mentioned above is 3. Thus, they induce ΔE of approximately +0.64 eV, implying that QB causes a VBM rise of 0.60 eV, very close to the ΔE data directly computed using DFT (~0.50 eV).

Hence, the interlayer QB interaction in Sb$_2$O$_3$ is weaker than that in MoS$_2$, attributed to the significant two-level interactions of the nearest neighbor Sp_z-Sp_z orbitals at the band edge in the latter (Fig. S6a); the former's band edge contains almost no out-of-plane orbitals (Fig. S8, S9), thus resulting in relatively weak interlayer two-level interactions. Therefore, to assess the interlayer band edge QB degree of a system, a rough judgment can be made by observing the orbital components and weights of the band edge-projected bands; generally, systems with stronger QB require larger weights of out-of-plane orbitals. For an accurate assessment of the QB degree, it is essential to first accurately identify the QB type at the band edge and then examine the contribution of k-COHP for the interlayer nearest or next-nearest atom pairs to ΔE.

Table S3: The band splitting of bilayer MoS$_2$ and bilayer Sb$_2$O$_3$ caused by interlayer QB interactions and its contribution decomposition. The t is k-COHP, unlike the general expression; positive values here represent antibonding and negative values represent bonding. Positive values of ΔE indicate an upward shift in energy levels, while negative values indicate a downward shift in energy levels. The N is the equivalent number of the interlayer atom pairs.

k-COHP	2L-MoS$_2$ VBM	2L-Sb$_2$O$_3$ CBM		2L-Sb$_2$O$_3$ VBM	
t (total)	S-S +0.2144	Sb-Sb -0.0193	Sb-O +0.0358	O-O +0.0017	Sb-O -0.0012
t (major contribution)	p_z - p_z 0.1855	p_z - p_z -0.0082	p_z - p_z +0.0175	p_x - p_x +0.0006	p_y - p_y -0.0008
	p_z - s 0.0159	p_z - p_y -0.0051	p_z - s +0.0149	p_z - p_x +0.0004	p_x - p_x -0.0002
$\triangle E$ type	Fig. S7a	Fig. S7b	Fig. S7c	Fig. S7a	Fig. S7c
N	3	6	6	6	6
$\triangle E$ formula	3t	6t	$(6t)^2/E_{diff}$	6t	$(6t)^2/E_{diff}$

$\triangle E$ (k-COHP)	+0.6432	-0.1158	+0.0154	+0.0102	≈ 0
$\triangle E$ (DFT)	+0.50	-0.06		-0.026	

Table S4: k-COHP with orbital decomposition of the interlayer S-S atomic pair in the VBM of bilayer MoS_2.

	s	p_y	p_z	p_x
s	-0.0029	0.0000	0.0159	0.0000
p_y	0.0000	0.0000	0.0000	0.0000
p_z	0.0159	0.0000	0.1855	0.0000
p_x	0.0000	0.0000	0.0000	0.0000

Table S5: k-COHP with orbital decomposition of the interlayer O-O atomic pair in the VBM of bilayer Sb_2O_3.

	s	p_y	p_z	p_x
s	0.0000	-0.0001	0.0000	0.0000
p_y	0.0000	-0.0001	0.0000	0.0000
p_z	0.0000	-0.0001	0.0000	-0.0004
p_x	0.0000	-0.0004	0.0000	-0.0006

Table S6: k-COHP with orbital decomposition of the interlayer Sb-Sb atomic pair in the CBM of bilayer Sb_2O_3.

	s	p_y	p_z	p_x
s	0.0000	0.0000	-0.0016	0.0000
p_y	0.0003	0.0005	0.0021	0.0000
p_z	-0.0017	-0.0051	-0.0082	-0.0002
p_x	-0.0003	0.0016	-0.0066	0.0000

Table S7: k-COHP with orbital decomposition of the interlayer Sb-O atomic pair in the VBM of bilayer Sb_2O_3.

	s	p_y	p_z	p_x
s	0.0000	0.0000	0.0000	0.0000
p_y	0.0000	-0.0008	0.0000	-0.0001
p_z	0.0000	0.0000	0.0000	0.0000
p_x	0.0000	0.0000	0.0000	-0.0002

Table S8: k-COHP with orbital decomposition of the interlayer Sb-O atomic pair in the CBM of bilayer Sb_2O_3.

	s	p_y	p_z	p_x
s	0.0004	0.0000	0.0011	-0.0001
p_y	0.0005	0.0004	0.0004	0.0002

p_z	0.0149	-0.0008	0.0175	-0.0028
p_x	0.0015	-0.0001	0.0014	0.0014

12. Analyses of surface ionic effect on the ionic dielectric constant

Table S9: Atomic Born effective charge and interatom force constant matrix elements for 1L and bulk α-Sb$_2$O$_3$ and h-BN. O1/O2 and Sb1/Sb2 atoms are labeled in Figure 4 of the main text.

		Z_{zz}^{*O1}	Z_{zz}^{*O2}	Z_{zz}^{*Sb1}	Z_{zz}^{*Sb2}	Φ_{zz}^{Sb1O1} (eV/A^2)	Φ_{zz}^{O1Sb2} (eV/A^2)	Φ_{zz}^{Sb2O2} (eV/A^2)
α-Sb$_2$O$_3$	1L	-0.76	-0.36	+0.72	+0.88	-6.16	-11.69	-2.22
	bulk	-2.49	-1.50	+2.01	+3.32	-5.47	-5.47	-2.59
		Z_{zz}^{*N}		Z_{zz}^{*B}		Φ_{zz}^{BN}		
h-BN	1L	-0.25		+0.25		-5.06		
	bulk	-0.66		+0.66		-4.85		

13. Interface leakage current between few-layer α- Sb$_2$O$_3$ dielectric and typical 2D semiconductor channel

Table S10: Leakage current in the *n*-MOS at 300 K

2D semiconductor	Dielectric	N_L	Leakage Current Density (A/cm^2)		
			Thermionic	Direct	Total
MoS$_2$	Sb$_2$O$_3$	1	1.89980×10^{-21}	9.29140×10^{5}	9.29140×10^{5}
		2	1.89978×10^{-21}	1.30424×10^{2}	1.30424×10^{2}
		3	1.89977×10^{-21}	3.21700×10^{-2}	3.21700×10^{-2}
		4	1.89977×10^{-21}	1.35514×10^{-5}	1.35514×10^{-5}
		5	1.89976×10^{-21}	5.50229×10^{-9}	5.50229×10^{-9}
MoSe$_2$	Sb$_2$O$_3$	1	7.71020×10^{-16}	2.03815×10^{6}	2.03815×10^{6}
		2	7.71011×10^{-16}	8.54974×10^{2}	8.54974×10^{2}
		3	7.71008×10^{-16}	6.30753×10^{-1}	6.30753×10^{-1}
		4	7.71005×10^{-16}	7.62495×10^{-4}	7.62495×10^{-4}
		5	7.71004×10^{-16}	9.08207×10^{-7}	9.08207×10^{-7}
MoTe$_2$	Sb$_2$O$_3$	1	5.23511×10^{-13}	3.12190×10^{6}	3.12190×10^{6}
		2	5.23505×10^{-13}	2.46454×10^{3}	2.46454×10^{3}
		3	5.23502×10^{-13}	3.42322×10^{0}	3.42322×10^{0}
		4	5.23500×10^{-13}	7.60808×10^{-3}	7.60808×10^{-3}
		5	5.23500×10^{-13}	1.68723×10^{-5}	1.68723×10^{-5}
WS$_2$	Sb$_2$O$_3$	1	7.73781×10^{-15}	2.36408×10^{6}	2.36408×10^{6}
		2	7.73772×10^{-15}	1.23094×10^{3}	1.23094×10^{3}
		3	7.73768×10^{-15}	1.12736×10^{0}	1.12736×10^{0}
		4	7.73766×10^{-15}	1.68000×10^{-3}	1.68000×10^{-3}
		5	7.73765×10^{-15}	2.47200×10^{-6}	2.47200×10^{-6}
WSe$_2$	Sb$_2$O$_3$	1	3.06927×10^{-10}	4.83639×10^{6}	4.83639×10^{6}
		2	3.06923×10^{-10}	7.65381×10^{3}	7.65381×10^{3}
		3	3.06922×10^{-10}	2.13219×10	2.13219×10
		4	3.06921×10^{-10}	9.25883×10^{-2}	9.25883×10^{-2}
		5	3.06920×10^{-10}	4.06799×10^{-4}	4.06799×10^{-4}
BP	Sb$_2$O$_3$	1	3.54801×10^{-17}	1.67871×10^{6}	1.67871×10^{6}
		2	3.54797×10^{-17}	5.33560×10^{2}	5.33560×10^{2}
		3	3.54796×10^{-17}	2.98193×10^{-1}	2.98193×10^{-1}
		4	3.54794×10^{-17}	2.75940×10^{-4}	2.75940×10^{-4}
		5	3.54794×10^{-17}	2.50205×10^{-7}	2.50205×10^{-7}

Table S11: Leakage current in the *p*-MOS at 300 K

2D semiconductor	dielectric	N_L	Leakage Current Density (A/cm^2)		
			Thermionic	Direct	Total
MoS$_2$	Sb$_2$O$_3$	1	1.16494×10^{-6}	2.72403×10^{6}	2.72403×10^{6}
		2	1.16493×10^{-6}	3.89254×10^{3}	3.89254×10^{3}
		3	1.16492×10^{-6}	9.79071×10^{0}	9.79071×10^{0}
		4	1.16492×10^{-6}	3.85300×10^{-2}	3.85400×10^{-2}
		5	1.16491×10^{-6}	1.53139×10^{-4}	1.54304×10^{-4}
MoSe$_2$	Sb$_2$O$_3$	1	6.36673×10^{-15}	4.01443×10^{5}	4.01443×10^{5}
		2	6.36666×10^{-15}	3.53079×10^{1}	3.53079×10
		3	6.36663×10^{-15}	5.45552×10^{-3}	5.45552×10^{-3}
		4	6.36661×10^{-15}	1.46484×10^{-6}	1.46484×10^{-6}
		5	6.36660×10^{-15}	3.75627×10^{-10}	3.75633×10^{-10}
MoTe$_2$	Sb$_2$O$_3$	1	2.85822×10^{-24}	6.78114×10^{4}	6.78114×10^{4}
		2	2.85819×10^{-24}	6.20386×10^{-1}	6.20386×10^{-1}
		3	2.85817×10^{-24}	9.95528×10^{-6}	9.95528×10^{-6}
		4	2.85816×10^{-24}	3.02273×10^{-10}	3.02273×10^{-10}
		5	2.85816×10^{-24}	8.37763×10^{-15}	8.37763×10^{-15}
WS$_2$	Sb$_2$O$_3$	1	5.28309×10^{-11}	9.46943×10^{5}	9.46943×10^{5}
		2	5.28303×10^{-11}	2.69195×10^{2}	2.69195×10^{2}
		3	5.28300×10^{-11}	1.34550×10^{-1}	1.34550×10^{-1}
		4	5.28299×10^{-11}	1.11821×10^{-4}	1.11821×10^{-4}
		5	5.28298×10^{-11}	9.08570×10^{-8}	9.09098×10^{-8}
WSe$_2$	Sb$_2$O$_3$	1	5.67661×10^{-19}	1.78649×10^{5}	1.78649×10^{5}
		2	5.67654×10^{-19}	5.49202×10^{0}	5.49202×10^{0}
		3	5.67651×10^{-19}	2.96389×10^{-4}	2.96389×10^{-4}
		4	5.67650×10^{-19}	2.89167×10^{-8}	2.89167×10^{-8}
		5	5.67649×10^{-19}	2.63833×10^{-12}	2.63833×10^{-12}
BP	Sb$_2$O$_3$	1	6.22805×10^{-19}	1.80035×10^{5}	1.80035×10^{5}
		2	6.22798×10^{-19}	5.58934×10^{0}	5.58934×10^{0}
		3	6.22795×10^{-19}	3.04626×10^{-4}	3.04626×10^{-4}
		4	6.22793×10^{-19}	3.00034×10^{-8}	3.00034×10^{-8}
		5	6.22792×10^{-19}	2.76409×10^{-12}	2.76409×10^{-12}

Table S12: Leakage current in the *n*-MOS at 400 K

2D semiconductor	Dielectric	N_L	Leakage Current Density (A/cm^2)		
			Thermionic	Tunneling	Total
MoS$_2$	Sb$_2$O$_3$	1	2.95944×10^{-15}	9.29140×10^{5}	9.29140×10^{5}
		2	2.95942×10^{-15}	1.30424×10^{2}	1.30424×10^{2}
		3	2.95941×10^{-15}	3.21733×10^{-2}	3.21733×10^{-2}
		4	2.95940×10^{-15}	1.35514×10^{-5}	1.35514×10^{-5}
		5	2.95939×10^{-15}	5.50229×10^{-9}	5.50229×10^{-9}
MoSe$_2$	Sb$_2$O$_3$	1	1.11779×10^{-11}	1.80363×10^{6}	1.80363×10^{-6}
		2	1.11778×10^{-11}	6.34834×10^{2}	6.34834×10^{2}
		3	1.11778×10^{-11}	3.92926×10^{-1}	3.92926×10^{-1}
		4	1.11778×10^{-11}	4.01142×10^{-4}	4.01142×10^{-4}
		5	1.11778×10^{-11}	4.02100×10^{-7}	4.02111×10^{-7}
MoTe$_2$	Sb$_2$O$_3$	1	1.11284×10^{-9}	2.67620×10^{6}	2.67620×10^{6}
		2	1.11283×10^{-9}	1.67438×10^{-3}	1.67438×10^{3}
		3	1.11283×10^{-9}	1.84290×10^{0}	1.84290×10^{0}
		4	1.11283×10^{-9}	3.27409×10^{-3}	3.27409×10^{-3}
		5	1.11282×10^{-9}	5.77723×10^{-6}	5.77834×10^{-6}
WS$_2$	Sb$_2$O$_3$	1	2.68313×10^{-10}	2.36408×10^{6}	2.36408×10^{6}
		2	2.68311×10^{-10}	1.23094×10^{3}	1.23094×10^{3}
		3	2.68310×10^{-10}	1.12736×10^{0}	1.12736×10^{0}
		4	2.68309×10^{-10}	1.67816×10^{-3}	1.67816×10^{-3}
		5	2.68309×10^{-10}	2.47200×10^{-6}	2.47227×10^{-6}
WSe$_2$	Sb$_2$O$_3$	1	9.92412×10^{-8}	4.00691×10^{6}	4.00691×10^{6}
		2	9.92404×10^{-8}	4.66792×10^{3}	4.66792×10^{3}
		3	9.92400×10^{-8}	9.57053×10^{0}	9.57053×10^{0}
		4	9.92398×10^{-8}	3.09411×10^{-2}	3.09412×10^{-2}
		5	9.92396×10^{-8}	1.00594×10^{-4}	1.00693×10^{-4}
BP	Sb$_2$O$_3$	1	4.72789×10^{-12}	1.67871×10^{6}	1.67871×10^{6}
		2	4.72785×10^{-12}	5.33560×10^{2}	5.33560×10^{2}
		3	4.72783×10^{-12}	2.98193×10^{-1}	2.98193×10^{-1}
		4	4.72782×10^{-12}	2.75940×10^{-4}	2.75940×10^{-4}
		5	4.72781×10^{-12}	2.50205×10^{-7}	2.50210×10^{-7}

2

Table S13: Leakage current in the *p*-MOS at 400 K

2D semiconductor	dielectric	N_L	Leakage Current Density (A/cm^2)		
			Thermionic	Tunneling	Total
MoS$_2$	Sb$_2$O$_3$	1	4.11667×10^{-4}	2.72403×10^{6}	2.72403×10^{6}
		2	4.11664×10^{-4}	3.89254×10^{3}	3.89254×10^{3}
		3	4.11662×10^{-4}	9.79071×10^{0}	9.79112×10^{0}
		4	4.11661×10^{-4}	3.85342×10^{-2}	3.89459×10^{-2}
		5	4.11661×10^{-4}	1.53139×10^{-4}	5.64800×10^{-4}
MoSe$_2$	Sb$_2$O$_3$	1	2.61671×10^{-10}	4.01443×10^{5}	4.01443×10^{5}
		2	2.61669×10^{-10}	3.53079×10^{1}	3.53079×10^{1}
		3	2.61668×10^{-10}	5.45552×10^{-3}	5.45552×10^{-3}
		4	2.61668×10^{-10}	1.46484×10^{-6}	1.46510×10^{-6}
		5	2.61667×10^{-10}	3.75627×10^{-10}	6.37294×10^{-10}
MoTe$_2$	Sb$_2$O$_3$	1	8.25597×10^{-16}	9.69648×10^{4}	9.69648×10^{4}
		2	8.25590×10^{-16}	1.38117×10^{0}	1.38117×10^{0}
		3	8.25587×10^{-16}	3.45181×10^{-5}	3.45181×10^{-5}
		4	8.25585×10^{-16}	1.60535×10^{-9}	1.60535×10^{-9}
		5	8.25584×10^{-16}	6.87558×10^{-14}	6.95814×10^{-14}
WS$_2$	Sb$_2$O$_3$	1	2.27502×10^{-7}	9.46943×10^{5}	9.46943×10^{5}
		2	2.27500×10^{-7}	2.69195×10^{2}	2.69195×10^{2}
		3	2.27499×10^{-7}	1.34549×10^{-1}	1.34549×10^{-1}
		4	2.27499×10^{-7}	1.11821×10^{-4}	1.12048×10^{-4}
		5	2.27498×10^{-7}	9.08570×10^{-8}	3.18355×10^{-7}
WSe$_2$	Sb$_2$O$_3$	1	3.20781×10^{-13}	1.84500×10^{5}	1.84500×10^{5}
		2	3.20778×10^{-13}	5.90969×10^{0}	5.90969×10^{0}
		3	3.20777×10^{-13}	3.32311×10^{-4}	3.32311×10^{-4}
		4	3.20776×10^{-13}	3.37297×10^{-8}	3.37300×10^{-8}
		5	3.20776×10^{-13}	3.20427×10^{-12}	3.52505×10^{-12}
BP	Sb$_2$O$_3$	1	2.57385×10^{-13}	1.80035×10^{5}	1.80035×10^{5}
		2	2.57383×10^{-13}	5.58934×10^{0}	5.58934×10^{0}
		3	2.57382×10^{-13}	3.04626×10^{-4}	3.04626×10^{-4}
		4	2.57381×10^{-13}	3.00034×10^{-8}	3.00037×10^{-8}
		5	2.57381×10^{-13}	2.76409×10^{-12}	3.02147×10^{-12}

14. Details on the definition of equivalent oxide thickness (EOT)

The performance of various dielectrics can be easily compared by calculating the equivalent oxide thickness (EOT). EOT is defined as the ratio of static dielectric constants between silicon dioxide (SiO₂) and the dielectric, considering a specified thickness (*t*), as expressed by the following formula:

$$\text{EOT} = \frac{\epsilon_{SiO_2}}{\epsilon_{diel}} t \tag{S1}$$

15. Tunneling effective mass in the leakage current

To estimate leakage current, we determine electron/hole tunneling effective mass by utilizing the out-of-plane effective masses derived from the energy dispersion diagram (*E–K*) across the conduction band minimum (for the electron effective mass) or the valence band maximum (for the hole effective mass) of the bulk. We extract the effective mass near the CBM and VBM by computing k-point paths along the out-of-plane direction in the bulk band structure, employing the PBE functional. The effective mass is determined by analyzing the band curvature along the out-of-plane direction, typically using the following mathematical expression:

$$\frac{1}{m^*} = \frac{1}{\hbar^2} \frac{d^2 E(k)}{dk^2} \tag{S2}$$

where *E(k)* is the band energy of the carrier at wave-vector *k* in the out-of-plane direction, and $\hbar$ is the reduced Plank constant. For few-layer α-Sb₂O₃, we use a tunneling mass of 1.037 m_0 for electrons and 1.684 m_0 for holes.

References

[1] S. Grimme, Semiempirical GGA-type density functional constructed with a long-range dispersion correction, J. Comput. Phys. **27**, 1787 (2006).

[2] S. Grimme, J. Antony, S. Ehrlich, and H. Krieg, A consistent and accurate ab initio parametrization of density functional dispersion correction (DFT-D) for the 94 elements H-Pu, J. Chem. Phys. **132**, 1 (2010).

[3] J. Klimeš, D. R. Bowler, and A. Michaelides, Van der Waals density functionals applied to solids, Phys. Rev. B **83**, 195131 (2011).

[4] H. Peng, Z.-H. Yang, J. P. Perdew, and J. Sun, Versatile van der Waals density functional based on a Meta-Generalized Gradient Approximation, Phys. Rev. X **6**, 041005 (2016).

[5] C. Svensson, Refinement of the crystal structure of cubic antimony trioxide, Sb_2O_3, Acta Crystallogr., Sect. B **31**, 2016 (1975).

[6] G. Rom, n-PÈrez and JM Soler, Efficient implementation of a van der Waals density functional: Application to double-wall Carbon nanotubes, Phys. Rev. Lett. **103**, 096102 (2009).

[7] K. Lee, É. D. Murray, L. Kong, B. I. Lundqvist, and D. C. Langreth, Higher-accuracy van der Waals density functional, Phys. Rev. B **82**, 081101 (2010).

[8] J. Klimeš, D. R. Bowler, and A. Michaelides, Chemical accuracy for the van der Waals density functional, J. Phys.: Condens. Matter **22**, 022201 (2009).

[9] J. Harl and G. Kresse, Accurate bulk properties from approximate many-body techniques, Phys. Rev. X **103**, 056401 (2009).

[10] T. Björkman, A. Gulans, A. V. Krasheninnikov, and R. M. J. a. p. a. Nieminen, Van der Waals bonding in layered compounds from advanced first-principles calculations, Phys. Rev. Lett. **108**, 235502 (2012).

[11] X. Sun, X. Li, J. Yang, J. Xi, R. Nelson, C. Ertural *et al.*, Achieving band convergence by tuning the bonding ionicity in n-type Mg_3Sb_2, J. Comput. Chem. **40**, 1693 (2019).

[12] R. Nelson, C. Ertural, J. George, V. L. Deringer, G. Hautier, and R. Dronskowski, LOBSTER: Local orbital projections, atomic charges, and chemical-bonding analysis from projector-augmented-wave-based density-functional theory, J. Comput. Chem. **41**, 1931 (2020).